Experimental validation of phase space conduits of transition between potential wells

Shane D. Ross,[1] Amir E. BozorgMagham,[1] Shibabrat Naik,[1,*] and Lawrence N. Virgin[2]

[1]*Engineering Mechanics Program, Virginia Tech, Blacksburg, Virginia 24061, USA*
[2]*Mechanical Engineering and Materials Science, Duke University, Durham, North Carolina 27708, USA*

A phase space boundary between transition and nontransition trajectories, similar to those observed in Hamiltonian systems with rank-1 saddles, is verified experimentally in a macroscopic system. We present a validation of the phase space flux across rank-1 saddles connecting adjacent potential wells, and we confirm the underlying phase space conduits that mediate the transition. Experimental regions of transition are found to agree with the theory to within 1%, suggesting the robustness of phase space conduits of transition in a broad array of two or more degrees of freedom experimental systems, despite the presence of small dissipation.

I. INTRODUCTION

Prediction of transition events and the determination of governing criteria has significance in many physical, chemical, and engineering systems where rank-1 saddles are present. Some examples of such systems include ionization of a hydrogen atom under an electromagnetic field in atomic physics [1], transport of defects in solid-state and semiconductor physics [2], isomerization of clusters [3], reaction rates in chemical physics [4,5], buckling modes in structural mechanics [6,7], ship motion and capsize [8–10], escape and recapture of comets and asteroids in celestial mechanics [11–13], and escape into inflation or recollapse to singularity in cosmology [14]. The theoretical criteria of transition and its agreement with laboratory experiment have been shown for one degree-of-freedom (DOF) systems [15–17]. Detailed experimental validation of the geometrical framework for predicting transition in higher dimensional phase space ($\geqslant 4$, that is, for two or more DOF systems) is still lacking. The geometric framework of phase space conduits in such systems, termed tube dynamics [11,12,18,19], has not been demonstrated in a laboratory experiment. It is noted that similar notions of transition were developed for idealized microscopic systems, particularly chemical reactions [1,20–22] under the terms of transition state and reactive island theory. However, investigations of the predicted phase space conduits of transition between wells in a multiwell system have stayed within the confines of numerical simulations. In this paper, we present a direct experimental validation of the accuracy of the phase space conduits, as well as the transition fraction obtained as a function of energy, in a four dimensional phase space using a controlled laboratory experiment of a macroscopic system.

In [23–25], experimental validation of global characteristics of one DOF Hamiltonian dynamics of scalar transport has been accomplished using direct measurement of the Poincaré stroboscopic sections using dye visualization of the fluid flow. In [23,24], the experimental and computational results of chaotic mixing were compared by measuring the observed and simulated distribution of particles, thus confirming the theory of chaotic transport in Hamiltonian systems for such systems. Our objective is to validate theoretical predictions of transition between potential wells in an exemplar experimental 2 DOF system, where qualitatively different global dynamics can occur. Our setup consists of a mass rolling on a multiwell surface that is representative of potential energy underlying systems that exhibit transition and escape behavior. The archetypal potential energy surface chosen has implications in transition, escape, and recapture phenomena in many of the aforementioned physical systems. In some of these systems, transition in the conservative case has been understood in terms of trajectories of a given energy crossing a hypersurface or transition state (bounded by a normally hyperbolic invariant manifold of geometry $\mathbb{S}^{2N-3}$ in N DOF). In this paper, for $N = 2$, trajectories pass inside a tubelike separatrix, which has the advantage of accommodating the inclusion of nonconservative forces such as stochasticity and damping [7,10]. The semianalytical geometry-based approach for identifying transition trajectories has also been considered for periodically forced 2 DOF systems in [26,27]. Our analytical approach here focuses on identifying separatrices from the unforced dynamics, and it generalizes to higher-dimensional phase space [5,28]. Based on the illustrative nature of our laboratory experiment of a 2 DOF mechanical system, and the generality of the framework to higher degrees of freedom [19], we envision that the geometric approach demonstrated here can apply to experiments regarding transition across rank-1 saddles in three or more DOF systems in many physical contexts.

II. SEPARATRICES in N DOF

To begin the mathematical description of the invariant manifolds that partition the $2N$-dimensional phase space, we perform a linear transformation of the underlying conservative Hamiltonian. This transformation involves a translation of the

*Author to whom all correspondence should be addressed: shiba@vt.edu

saddle equilibrium point to the origin and a linear change of coordinates that uses the eigenvectors of the linear system. The resulting Hamiltonian near the saddle has the quadratic (normal) form

$$H_2(q_1, p_1, \ldots, q_N, p_N) = \lambda q_1 p_1 + \sum_{k=2}^{N} \frac{\omega_k}{2}(q_k^2 + p_k^2), \quad (1)$$

where N is the number of degrees of freedom, λ is the real eigenvalue corresponding to the saddle coordinates (*reactive coordinates* for chemical reactions) spanned by (q_1, p_1), and ω_k are the frequencies associated with the center coordinates (*bath coordinates* for chemical reactions) spanned by the pair (q_k, p_k) for $k \in 2, \ldots, N$.

Next, by fixing the energy level to $h \in \mathbb{R}^+$ and constant $c \in \mathbb{R}^+$, we can define a codimension-1 region $\mathcal{R} \subset \mathbb{R}^{2N}$ in the full phase space by the conditions

$$H_2(q_1, p_2, \ldots, q_N, p_N) = h \quad \text{and} \quad |p_1 - q_1| \le c. \quad (2)$$

This implies that $\mathcal{R}$ is homeomorphic to the product of a $(2N - 2)$ sphere and an interval I, that is, $\mathcal{R} \cong \mathcal{S}^{2N-2} \times I$, where the $\mathcal{S}^{2N-2}$ is given by

$$\frac{\lambda}{4}(q_1 + p_1)^2 + \sum_{k=2}^{N} \frac{\omega_k}{2}(q_k^2 + p_k^2) = h + \frac{\lambda}{4}(p_1 - q_1)^2. \quad (3)$$

The sphere of $\mathcal{R}$ at the middle of the equilibrium region, where $p_1 - q_1 = 0$

$$\mathcal{N}_h^{2N-2} = \left\{ (q, p) | \lambda p_1^2 + \sum_{k=2}^{N} \frac{\omega_k}{2}(q_k^2 + p_k^2) = h \right\}, \quad (4)$$

corresponds to the transition state in chemical reactions (and other systems with similar Hamiltonian structure [7,10,11]).

The following phase space structures and their geometry are relevant for understanding transition across the saddle.

A. NHIM

The point $q_1 = p_1 = 0$ in the saddle projection corresponds to an invariant $(2N - 3)$ sphere, $\mathcal{M}_h^{2N-3}$, of periodic and quasiperiodic orbits in $\mathcal{R}$, and is given by

$$\sum_{k=2}^{N} \frac{\omega_k}{2}(q_k^2 + p_k^2) = h, \quad q_1 = p_1 = 0. \quad (5)$$

This is known as the *normally hyperbolic invariant manifold* (NHIM), which has the property that the manifold has a "saddlelike" stability in directions transverse to the manifold, and initial conditions on this surface evolve on it for $t \to \pm\infty$. The role of unstable periodic orbits in the four-dimensional phase space (or more generally the NHIM in the $2N$-dimensional phase space) in transition between potential wells is acting as an anchor for constructing the separatrices of transit and nontransit trajectories.

B. Separatrix

The four half-open segments on the axes, $q_1 p_1 = 0$, correspond to four high-dimensional cylinders of orbits asymptotic to this invariant $\mathbb{S}^{2N-3}$ either as time increases ($p_1 = 0$) or as time decreases ($q_1 = 0$). These are called *asymptotic* orbits and they form the stable and the unstable invariant manifolds of $\mathbb{S}^{2N-3}$. The stable manifolds, $\mathcal{W}_{\pm}^s(\mathbb{S}^{2N-3})$, are given by

$$\sum_{k=2}^{N} \frac{\omega_k}{2}(q_k^2 + p_k^2) = h, \quad q_1 = 0, \quad (6)$$

where $\pm$ denotes the left and right branches of the stable manifold attached to the NHIM. Similarly, unstable manifolds are constructed and are shown in the saddle space in Fig. 1 as four orbits labeled M. These form the "spherical cylinders" of orbits asymptotic to the invariant $(2N - 3)$ sphere. Topologically, both invariant manifolds have the structure of $(2N - 2)$-dimensional "tubes" ($\mathbb{S}^{2N-3} \times \mathbb{R}$) inside the $(2N - 1)$-dimensional energy surface. Thus, they separate two distinct types of motion: transit and nontransit trajectories. While a transition trajectory, passing from one region to another, lies inside the $(2N - 2)$-dimensional manifold, the nontransition trajectories, bouncing back to their current region of motion, are those outside the manifold.

For a value of the energy just above that of the saddle, the nonlinear motion in the equilibrium region $\mathcal{R}$ is qualitatively the same as the linearized picture above [5,29,30].
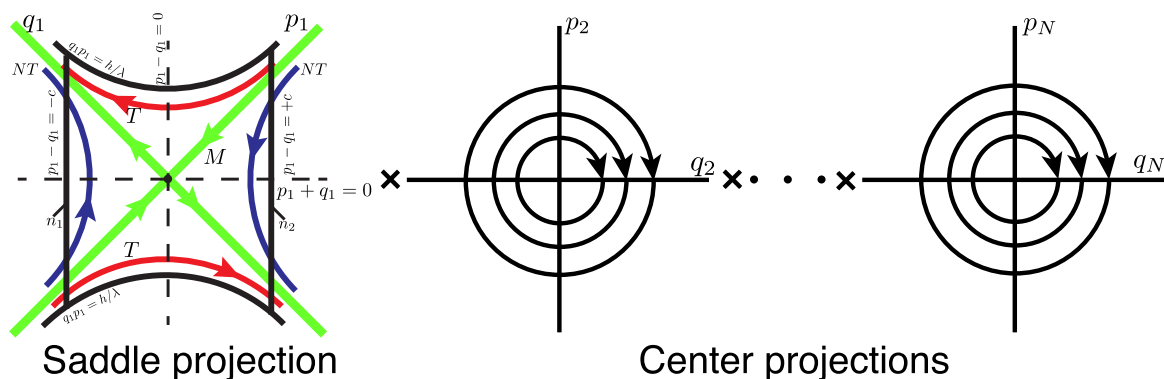

Saddle projection   Center projections

FIG. 1. The flow in the region $\mathcal{R}$ can be separated into saddle $\times$ center $\times \cdots \times$ center. On the left, the saddle projection is shown on the (q_1, p_1) plane. The NHIM (black dot at the origin), the asymptotic orbits on the stable and unstable manifolds (M), two transition trajectories (T), and two nontransition trajectories (NT).

For example, the NHIM for the nonlinear system, which corresponds to the $(2N - 3)$ sphere in (5) for the linearized system, is given by

$$
\mathcal{M}_h^{2N-3} = \left\{ (q, p)| \sum_{k=2}^{N} \frac{\omega_k}{2} (q_k^2 + p_k^2) \right.
$$
$$
\left. + f(q_2, p_2, \ldots, q_n, p_n) = h, \quad q_1 = p_1 = 0 \right\},
$$
(7)

where f is at least of third order. Here, $(q_2, p_2, \ldots, q_N, p_N)$ are normal form coordinates and are related to the linearized coordinates via a near-identity transformation. In the neighborhood of the equilibrium point, since the higher-order terms in f are negligible compared to the second-order terms, the $(2N - 3)$ sphere for the linear problem is a deformed sphere for the nonlinear problem. Moreover, since the NHIMs persist for higher energies, this deformed sphere $\mathcal{M}_h^{2N-3}$ still has stable and unstable invariant manifolds that are given by

$$
\mathcal{W}_{\pm}^S (\mathcal{M}_h^{2N-3}) = \left\{ (q, p)| \sum_{k=2}^{N} \frac{\omega_k}{2} (q_k^2 + p_k^2) \right.
$$
$$
\left. + f(q_2, p_2, \ldots, q_n, p_n) = h, \quad q_1 = 0 \right\},
$$

$$
\mathcal{W}_{\pm}^u (\mathcal{M}_h^{2N-3}) = \left\{ (q, p)| \sum_{k=2}^{N} \frac{\omega_k}{2} (q_k^2 + p_k^2) \right.
$$
$$
\left. + f(q_2, p_2, \ldots, q_n, p_n) = h, \quad p_1 = 0 \right\}.
$$
(8)

This geometric insight is useful for developing numerical methods for *globalization* of the invariant manifolds using numerical continuation [31].

Now, we briefly describe the techniques that can be used to quantify and visualize the high-dimensional invariant manifolds. For positive value of excess energy, one can use a normal form computation to obtain higher-order terms of (7) and (8). A brief overview of this approach is given in [32] along with applications and results obtained using the computational tool for the Hamiltonian normal form. Another approach is to sample points on these manifolds since the geometry of the manifold is known near the equilibrium point. One would start by taking Poincaré sections and using normal form theory that involves high-order expansions around a saddle × center ⋯ × center equilibrium. For example, in 3 DOF, the NHIM has topology $\mathbb{S}^3$ and thus a tube cross section on a 4D Poincaré section will have topology $\mathbb{S}^3$ for which it is possible to obtain an inside and outside. If $x = $ const defines the Poincaré section, then one can project the $\mathbb{S}^3$ structure to two transverse planes, (y, p_y) and (z, p_z). On each plane, the projection appears as a disk, but because of the $\mathbb{S}^3$ topology, any point in the (z, p_z) projection corresponds to a topological circle in the (y, p_y) (and vice versa), and from this one can determine which initial conditions are inside, and thus transit trajectories, as has been performed previously [28,33].
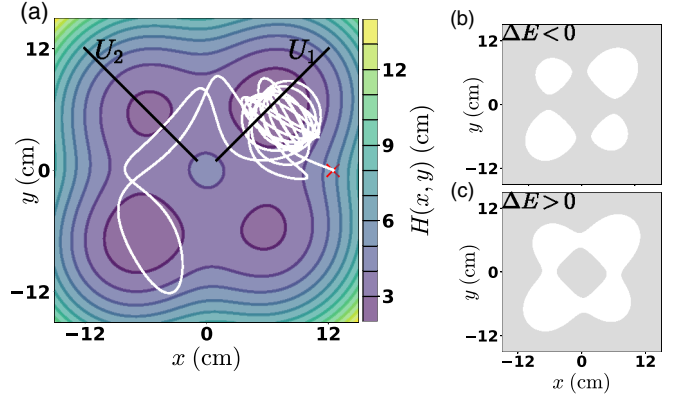

FIG. 2. (a) A typical experimental trajectory, shown in white, on the potential energy surface where the contours denote isoheights of the surface. This instance of the trajectory was traced by the ball released from rest, marked by a red cross. Parts (b) and (c) show the energetically accessible region projected on the configuration space in white for $\Delta E < 0$: $\Delta E = -100$ (cm/s)^2 and $\Delta E > 0$: $\Delta E = 100$ (cm/s)^2, respectively.

III. MODEL OF THE 2 DOF EXPERIMENTAL SYSTEM

The initial mathematical model of the transition behavior of a rolling ball on the surface, $H(x, y)$, shown in Fig. 5(b), is described in [34]. The equations of motion are obtained from the Hamiltonian, $\mathcal{H}(x, y, p_x, p_y) = T(x, y, p_x, p_y) + V(x, y)$, where mass factors out and where the kinetic energy (translational and rotational for a ball rolling without slipping) is

$$
T = \frac{5}{14} \frac{(1 + H_y^2) p_x^2 + (1 + H_x^2) p_y^2 - 2 H_x H_y p_x p_y}{1 + H_x^2 + H_y^2}, \quad (9)
$$

where $H_{(\cdot)} = \frac{\partial H}{\partial (\cdot)}$. The potential energy is $V(x, y) = gH(x, y)$, where $g = 981$ cm/s^2 is the gravitational acceleration, and the height function is

$$
H = \alpha(x^2 + y^2) - \beta(\sqrt{x^2 + \gamma} + \sqrt{y^2 + \gamma}) - \xi xy + H_0.
$$
(10)

This is the analytical function for the machined surface shown in Fig. 5(b) and the isoheights shown in Fig. 2(a). We use parameter values $(\alpha, \beta, \gamma, \xi, H_0) = (0.07, 1.017, 15.103, 0.006\,56, 12.065)$ in the appropriate units [31].

Let $\mathcal{M}(E)$ be the *energy manifold* in the 4D phase space given by setting the total energy equal to a constant, E, i.e., $\mathcal{M}(E) = \{(x, y, p_x, p_y) \subset \mathbb{R}^4 \mid \mathcal{H}(x, y, p_x, p_y) = E\}$. The projection of the energy manifold onto the (x, y) configuration space is the region of energetically possible motion for a mass with energy E, and is given by $M(E) = \{(x, y) \mid V(x, y) \leqslant E\}$. The boundary of $M(E)$ is the zero velocity curve and is defined as the locus of points in the (x, y) plane where the kinetic energy is zero. The mass is only able to move on the side of the curve where the kinetic energy is positive, shown as white regions in Figs. 2(b) and 2(c). The critical energy for transition, E_e, is the energy of the rank-1 saddle points in each bottleneck, which are all equal. This energy divides the global behavior of the mass into two cases,
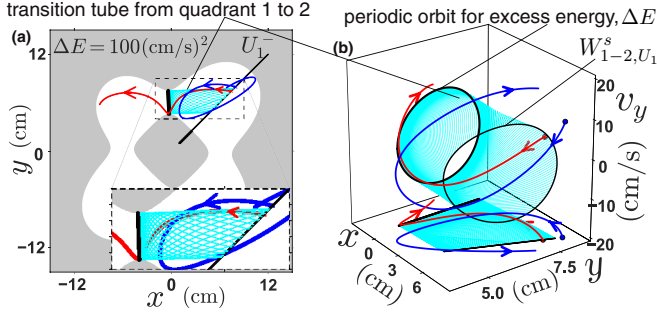
FIG. 3. (a) For a fixed excess energy, ΔE, above the critical value E_e, the permissible regions (in white) are connected by a bottleneck around the saddle equilibria. All motion from the well in quadrant 1 to quadrant 2 must occur through the interior of a stable manifold associated with an unstable periodic orbit in the bottleneck between the quadrants, seen as a 2D configuration space projection of the 3D energy manifold. We show the stable manifold (cyan) and the periodic orbit (black) for an excess energy of $\Delta E = 100$ (cm/s)^2. A trajectory crossing the U_1^- section inside the stable manifold will transition (red) into the quadrant 2 well, while one that is outside (blue) stays inside quadrant 1. The zoomed-in inset in the figure shows the structure of the manifold and how precisely the separatrix divides transition and nontransition trajectories. (b) In the (x, y, v_y) projection, the phase space conduit for imminent transition from quadrant 1 to 2 is the stable manifold (cyan) of geometry $\mathbb{R}^1 \times \mathbb{S}^1$ (i.e., a cylinder). The same example trajectories (red and blue) as in (a) that exhibit transition and nontransition behavior starting inside and outside the stable manifold, respectively, are shown in the 3D projection and projected on the (x, y) configuration space. A movie of a nested sequence of these manifolds can be found at Ref. [35].

according to the sign of the excess energy above the saddle, $\Delta E = E - E_e$:

Case 1. $\Delta E < 0$—the mass is safe against transition and remains inside the starting well since potential wells are not energetically connected [Fig. 2(b)].

Case 2. $\Delta E > 0$—the mass can transition by crossing the bottlenecks that open up around the saddle points, permitting transition between the potential wells [Figs. 2(c) and Fig. 3(a) show this case].

Thus, transition between wells can occur when $\Delta E > 0$, and this constitutes a necessary condition. The sufficient condition for transition to occur is when a trajectory enters a codimension-1 invariant manifold associated with the unstable periodic orbit in the bottleneck as shown by nontransition and transition trajectories in Fig. 3(a) [18]. In 2 DOF systems, the periodic orbit residing in the bottleneck has an invariant manifold that is codimension-1 in the energy manifold and has topology $\mathbb{R}^1 \times \mathbb{S}^1$, which is a cylinder or tube [31]. This implies that the transverse intersection of these manifolds with Poincaré surfaces-of-sections, U_1 and U_2, is topologically $\mathbb{S}^1$, a closed curve [7,10,18]. All the trajectories transitioning to a different potential well (or having just transitioned into the well) are inside a tube manifold, for example as shown in Fig. 3(b) [18,19]. For every $\Delta E > 0$, the tubes in phase space [or more precisely, within $\mathcal{M}(E)$] that lead to transition are the stable (and that lead to entry are the unstable) manifolds associated with the unstable periodic orbit of energy E. Thus, the mass's imminent transition
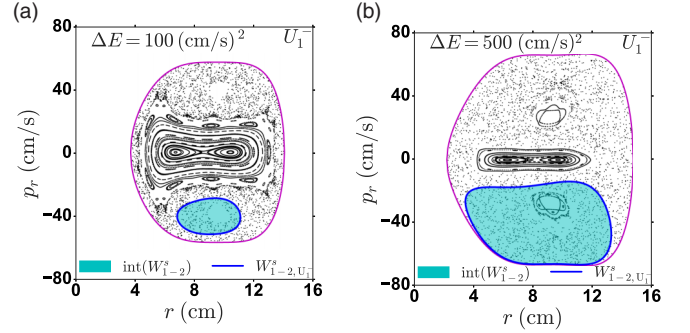

FIG. 4. Poincaré section, $P^- : U_1^- \to U_1^-$, of trajectories where $U_1^- := \{(r, p_r) \mid \theta = \pi/4, \ p_\theta > 0\}$, at excess energy (a) $\Delta E = 100$ (cm/s)^2 and (b) $\Delta E = 500$ (cm/s)^2. The blue curves with a cyan interior denote the intersection of the tube manifold (stable) associated with the unstable periodic orbit with U_1^-. It should be noted that these manifolds act as a boundary between transition and nontransition trajectories, and may include KAM tori spanning more than one well. The interior of the manifolds, $\text{int}(\cdot)$, denotes the region of imminent transition to the quadrant 2 from quadrant 1. A movie showing the Poincaré section for a range of excess energy can be found at Ref. [36].

between adjacent wells can be predicted by considering where it crosses U_1, as shown in Fig. 4, relative to the intersection of the tube manifold. Furthermore, nested energy manifolds have corresponding nested stable and unstable manifolds that mediate transition. To simplify analysis, we focus only on the transition of trajectories that intersect U_1 in the first quadrant. This surface-of-section is best described in polar coordinates $(r, \theta, p_r, p_\theta)$; $U_1^\pm = \{(r, p_r) \mid \theta = \frac{\pi}{4}, \ -\text{sgn}(p_\theta) = \pm 1\}$, where $+$ and $-$ denote motion to the right and left of the section, respectively [31]. This Hamiltonian flow on $U_1^\pm$ defines a symplectic map with typical features such as KAM tori and chaotic regions, shown in Fig. 4 for two values of excess energy.

Based on these phase space conduits that lead to transition, we would like to calculate what fraction of the energetically permissible trajectories will transition from or into a given well. This can be answered in part by calculating the transition rate of trajectories crossing the rank-1 saddle in the bottleneck connecting the wells. For computing this rate—surface integral of trajectories crossing a bounded surface per unit time—we use the geometry of the tube manifold cross section on the Poincaré section. For low excess energy, this computation is based on the theory of flux over a rank-1 saddle [37], which corresponds to the action integral around the periodic orbit at energy ΔE. By the Poincaré integral invariant [38], this action is preserved for symplectic maps, such as $P^\pm : U_1^\pm \to U_1^\pm$, and is equivalent to computing the area of the tube manifold's intersection with the surface-of-section. The transition fraction at each energy, $p_{\text{trans}}(\Delta E)$, is calculated by the fraction of energetically permissible trajectories at a given excess energy, ΔE, that will transition. This is given by the ratio of the cross sections on U_1 of the tube to the energy surface. The transition area, to leading order in ΔE [37], is given by $A_{\text{trans}} = T_{\text{po}} \Delta E$, where $T_{\text{po}} = 2\pi/\omega$ is the period of the periodic orbits of small energy in the bottleneck, where ω is the imaginary part of the complex-conjugate pair of eigenvalues resulting from the
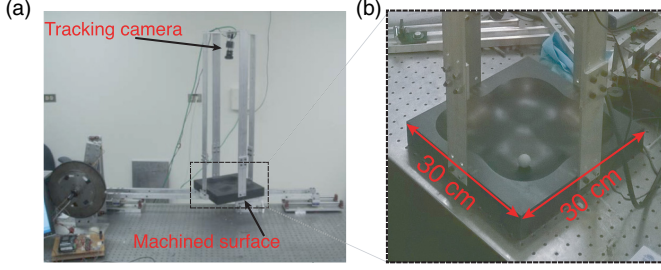
FIG. 5. (a), (b) Experimental apparatus showing the machined surface, tracking camera, and the rubber coated steel ball.

linearization about the saddle equilibrium point [37]. The area of the energy surface projection on U_1, to leading order in $\Delta E > 0$, is $A_E = A_0 + \tau \Delta E$, where

$$A_0 = 2 \int_{r_{\min}}^{r_{\max}} \sqrt{\frac{14}{5}[E_e - gH(r)]\left[1 + 4H_r^2(r)\right]} \, dr \quad (11)$$

$$\text{and } \tau = \int_{r_{\min}}^{r_{\max}} \sqrt{\frac{14}{5} \frac{\left[1 + 4H_r^2(r)\right]}{[E_e - gH(r)]}} \, dr. \quad (12)$$

The transition fraction, under the well-mixed assumption mentioned earlier, is given in 2 DOF by

$$p_{\text{trans}} = \frac{A_{\text{trans}}}{A_E} = \frac{T_{\text{po}}}{A_0} \Delta E \left(1 - \frac{\tau}{A_0}\Delta E + O(\Delta E^2)\right). \quad (13)$$

For small positive excess energy, the predicted growth rate is $T_{\text{po}}/A_0 \approx 0.87 \times 10^{-3}$ (s/cm)^2. For larger values of ΔE, the cross-sectional areas are computed numerically using Green's theorem; see Fig. 6(b).

As with any physical experiment, there is dissipation present, but over the timescale of interest, the motion approximately conserves energy. We compare δE, the typical energy lost during a transition, with the typical excess energy, $\Delta E > 0$, when transitions are possible. The timescale of interest, t_{trans}, corresponds to the time between crossing U_1 and transitioning across the saddle into a neighboring well. The energy loss over t_{trans} in terms of the measured damping ratio $\zeta \approx 0.025$ is $\delta E \approx \pi \zeta v^2(\Delta E)$, where the squared-velocity $v^2(\Delta E)$ is approximated through the total energy. For our experimental trajectories, all starting at $\Delta E > 1000$ (cm/s)^2, we find $\delta E / \Delta E \ll 1$, suggesting the appropriateness of the assumption of short-time conservative dynamics to study transition between wells [7,10].

IV. EXPERIMENTAL SETUP

We designed a surface that has four wells, one in each quadrant, with saddles connecting the neighboring quadrants [shown in Fig. 5(b)]. The surface has four stable and five saddle (four rank-1 and one rank-2) equilibrium points. Inter-well first-order transitions are defined as crossing the rank-1 saddles between the wells. On this high-precision machined surface, accurate to within 0.003 mm and made using stock polycarbonate, a small rubber-coated spherical steel mass released from rest can roll without slipping under the influence of gravity. The mass is released from different locations on the machined surface to generate experimental trajectories.
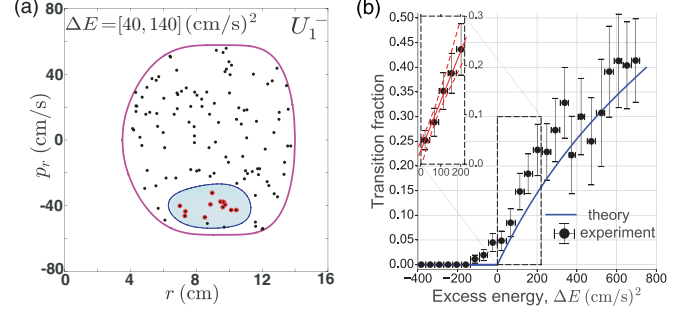

FIG. 6. (a) On the Poincaré section, U_1^-, we show a narrow range of energy [$\Delta E \in (40, 140)$ (cm/s)^2] and label intersecting trajectories as no transition (black) and imminent transition (red) to quadrant 2, based on their measured behavior. The stable invariant manifold associated with the bottleneck periodic orbit at excess energy, $\Delta E = 140$ (cm/s)^2, intersects the Poincaré section, U_1^-, along the blue curve. Its interior is shown in cyan and includes the experimental transition trajectories. The outer closed curve (magenta) is the intersection of the boundary of the energy surface $\mathcal{M}(\Delta E)$ with U_1^-. (b) Transition fraction of trajectories as a function of excess energy above the saddle. The theoretical result is shown (blue curve) and experimental values are shown as filled circles (black) with error bars. For small excess energy above critical ($\Delta E = 0$), the transition fraction shows linear growth (see inset) with slope $1.0 \pm 0.23 \times 10^{-3}$ (s/cm)^2 and shows agreement with the analytical result (13). A movie of increasing transition area on the Poincaré section, U_1^-, can be found at Ref. [39].

The mass is tracked using a Prosilica GC640 digital camera mounted on a rigid frame attached to the surface as shown in Fig. 5(a), with a pixel resolution of about 0.16 cm. The tracking is done by capturing black and white images at 50 Hz, and calculating the coordinates of the mass's geometrical center. We recorded 120 experimental trajectories of about 10 s long, only using data after waiting at least the Lyapunov time of ≈ 0.4 s [34] ensuring that the trajectories were well-mixed in the phase space. To analyze the fraction of trajectories that leave or enter a well, we obtain approximately 4000 intersections with a Poincaré surface-of-section, U_1, shown as a black line, for the analyzed range of energy. One such trajectory is shown in white in Fig. 2(a). These intersections are then sorted according to energy. The intersection points on U_1 are classified as a transition from quadrant 1 to 2 if the trajectory, followed forward in time, leaves quadrant 1. A total of 400 transition events were recorded.

V. RESULTS

For each of the recorded trajectories, we detect intersections with U_1 and determine the instantaneous ΔE. Grouping intersection points by energy [e.g., Fig. 6(a)], we get an experimental transition fraction, Fig. 6(b), by dividing points that transitioned by the total in each energy range. Despite the experimental uncertainty from the image analysis, agreement between observed and predicted values is satisfactory. In fact, a linear fit of the experimental results for small excess energy gives a slope close to that predicted by (13) within the margin of error. Furthermore, the clustering of observed transitioning trajectories in each energy range, as in Fig. 6(a), is consistent

with the theory of tube dynamics. The predicted transition regions in each energy range account for more than 99% of the observed transition trajectories.

VI. CONCLUSIONS

We considered a macroscopic 2 DOF experimental system showing transitions between potential wells and a dynamical systems theory of the conduits that mediate those transitions [7,10,18]. The experimental validation presented here confirms the robustness of the conduits between multistable regions, even in the presence of nonconservative forces, providing a strong footing for predicting transitions in a wide range of physical systems. Given the fragility of other structures to dissipation (for example, KAM tori and periodic orbits), these phase space conduits of transition may be among the most robust features to be found in experiments of autonomous multiple DOF systems. Furthermore, this study lays the groundwork for experimental validation for an $N = 3$ or more DOF system, such as ship dynamics [8–10,40], buckling of beams [7] and geodesic lattice domes, hanging roller pins, isomerization, and roaming reactions [41,42].

[1] C. Jaffé, D. Farrelly, and T. Uzer, Phys. Rev. Lett. **84**, 610 (2000).

[2] B. Eckhardt, J. Phys. A **28**, 3469 (1995).

[3] T. Komatsuzaki and R. S. Berry, Proc. Natl. Acad. Sci. (U.S.A.) **98**, 7666 (2001).

[4] T. Komatsuzaki and R. S. Berry, J. Chem. Phys. **110**, 9160 (1999).

[5] S. Wiggins, L. Wiesenfeld, C. Jaffé, and T. Uzer, Phys. Rev. Lett. **86**, 5478 (2001).

[6] P. Collins, G. S. Ezra, and S. Wiggins, Phys. Rev. E **86**, 056218 (2012).

[7] J. Zhong, L. N. Virgin, and S. D. Ross, Int. J. Mech. Sci. **149**, 413 (2018).

[8] L. N. Virgin, Dyn. Stab. Syst. **4**, 56 (1989).

[9] J. M. T. Thompson and J. R. de Souza, Proc. R. Soc. Lond. A **452**, 2527 (1996).

[10] S. Naik and S. D. Ross, Commun. Nonlin. Sci. **47**, 48 (2017).

[11] C. Jaffé, S. D. Ross, M. W. Lo, J. E. Marsden, D. Farrelly, and T. Uzer, Phys. Rev. Lett. **89**, 011101 (2002).

[12] M. Dellnitz, O. Junge, M. W. Lo, J. E. Marsden, K. Padberg, R. Preis, S. D. Ross, and B. Thiere, Phys. Rev. Lett. **94**, 231102 (2005).

[13] S. D. Ross, in *Libration Point Orbits and Applications*, edited by G. Gómez, M. W. Lo, and J. J. Masdemont (World Scientific, Singapore, 2003), pp. 637–652.

[14] H. P. de Oliveira, A. M. Ozorio de Almeida, I. Damião Soares, and E. V. Tonini, Phys. Rev. D **65**, 083511 (2002).

[15] L. N. Virgin and L. A. Cartee, Int. J. Nonlin. Mech. **26**, 449 (1991).

[16] J. A. Gottwald, L. N. Virgin, and E. H. Dowell, J. Sound Vib. **187**, 133 (1995).

[17] J. Novick, M. L. Keeler, J. Giefer, and J. B. Delos, Phys. Rev. E **85**, 016205 (2012).

[18] W. S. Koon, M. W. Lo, J. E. Marsden, and S. D. Ross, Chaos **10**, 427 (2000).

[19] F. Gabern, W. S. Koon, J. E. Marsden, S. D. Ross, and T. Yanao, Few-Body Syst. **38**, 167 (2006).

[20] A. M. Ozorio de Almeida, N. De Leon, M. A. Mehta, and C. C. Marston, Physica D **46**, 265 (1990).

[21] N. De Leon, M. A. Mehta, and R. Q. Topper, J. Chem. Phys. **94**, 8310 (1991).

[22] C. C. Marston and N. De Leon, J. Chem. Phys. **91**, 3392 (1989).

[23] O. Baskan, M. F. M. Speetjens, G. Metcalfe, and H. J. H. Clercx, Chaos **25**, 103106 (2015).

[24] O. Baskan, M. F. M. Speetjens, G. Metcalfe, and H. J. H. Clercx, Eur. J. Mech. B/Fluids **57**, 1 (2016).

[25] A. Figueroa, S. Cuevas, and E. Ramos, J. Fluid Mech. **815**, 415 (2017).

[26] E. S. Gawlik, J. E. Marsden, P. C. Du Toit, and S. Campagnola, Celest. Mech. Dynam. Astron. **103**, 227 (2009).

[27] K. Onozaki, H. Yoshimura, and S. D. Ross, Adv. Space Res. **60**, 2117 (2017).

[28] F. Gabern, W. S. Koon, J. E. Marsden, and S. D. Ross, Physica D **211**, 391 (2005).

[29] J. Moser, Commun. Pure Appl. Math. **11**, 257 (1958).

[30] H. Waalkens and S. Wiggins, Reg. Chaotic Dyn. **15**, 1 (2010).

[31] See Supplemental Material at http://link.aps.org/supplemental/10.1103/PhysRevE.98.052214 for derivation of the equations of motion and the computational approach used to obtain the invariant manifolds.

[32] S. Wiggins, in *IUTAM Symposium on Hamiltonian Dynamics, Vortex Structures, Turbulence*, edited by A. V. Borisov, V. V. Kozlov, I. S. Mamaev, and M. A. Sokolovskiy (Springer, Dordrecht, 2008), pp. 189–203. A. D. Burbanks, S. Wiggins, H. Waalkens, and R. Schubert, Background and documentation of software for computing hamiltonian normal forms (2008), software for normal form is available at https://github.com/Peter-Collins/NormalForm.

[33] G. Gómez, W. S. Koon, M. W. Lo, J. E. Marsden, J. Masdemont, and S. D. Ross, Nonlinearity **17**, 1571 (2004).

[34] L. N. Virgin, T. C. Lyman, and R. B. Davis, Am. J. Phys. **78**, 250 (2010).

[35] https://youtu.be/gMqrFX2JkLU.

[36] https://youtu.be/sNvgXCrX6oo.

[37] R. S. MacKay, Phys. Lett. A **145**, 425 (1990).

[38] J. D. Meiss, Rev. Mod. Phys. **64**, 795 (1992).

[39] https://youtu.be/YZKYx0N9Zug.

[40] L. McCue and A. Troesch, Ocean Engineering **32**, 1608 (2005); **33**, 1796 (2006).

[41] F. A. L. Mauguière, P. Collins, G. S. Ezra, S. C. Farantos, and S. Wiggins, Theor. Chem. Acc. **133** (2014).

[42] J. M. Bowman and P. L. Houston, Chem. Soc. Rev. **46**, 7615 (2017).

SUPPLEMENTAL MATERIAL
Experimental validation of phase space conduits of transition between potential wells

Shane D. Ross[1], Amir E. BozorgMagham[1], Shibabrat Naik [*1], and Lawrence N. Virgin[2]

[1]Engineering Mechanics Program, Virginia Tech, Blacksburg, Virginia 24061, USA
[2]Mechanical Engineering and Materials Science, Duke University, Durham, NC 27708, USA

1   Equations of motion

Let us consider a ball is rolling on a smooth surface described by the analytical function

$$H(x,y) = \alpha(x^2 + y^2) - \beta\left(\sqrt{x^2 + \gamma} + \sqrt{y^2 + \gamma}\right) - \xi xy + H_0 \tag{1}$$

where $\alpha = 0.07, \beta = 1.017, \gamma = 15.103, \xi = 0.00656$ are constant parameters in appropriate units, and $H_0 = 12.065$ cm, $g = 981$ cm/s^2. The height of the ball, z, is restricted to the surface, $z = H(x,y)$, at the configuration space coordinates, (x,y). Thus

$$\frac{dz}{dt} = \dot{x}H_x + \dot{y}H_y, \text{ where } H_x = \frac{\partial H}{\partial x}, \ H_y = \frac{\partial H}{\partial y} \tag{2}$$

The translational and rotational energy for a ball is given by

$$E_{\text{trans}} = \frac{m}{2}\left(\dot{x}^2 + \dot{y}^2 + \dot{z}^2\right) = \frac{m}{2}\left(\dot{x}^2 + \dot{y}^2 + (\dot{x}H_x + \dot{y}H_y)^2\right) \tag{3}$$

$$E_{\text{rot}} = \frac{1}{2}I\omega^2 = \frac{1}{2}\left(\frac{2}{5}mr^2\right)\omega^2 = \frac{m}{5}v^2 = \frac{m}{5}\left(\dot{x}^2 + \dot{y}^2 + (\dot{x}H_x + \dot{y}H_y)^2\right) \tag{4}$$

The total kinetic energy is a combination of translational and rotational kinetic energy for a ball rolling without slipping, and is given by

$$T(x,y,\dot{x},\dot{y}) = E_{\text{kinetic}} = E_{\text{trans}} + E_{\text{rot}} = \frac{1}{2}\frac{7}{5}m\left(\dot{x}^2 + \dot{y}^2 + (H_x\dot{x} + H_y\dot{y})^2\right)$$

$$T(x,y,\dot{x},\dot{y}) = \frac{1}{2}m\begin{bmatrix}\dot{x}\\\dot{y}\end{bmatrix}^T \frac{7}{5}\begin{bmatrix}(1+H_x^2) & H_xH_y \\ H_xH_y & (1+H_y^2)\end{bmatrix}\begin{bmatrix}\dot{x}\\\dot{y}\end{bmatrix} \tag{5}$$

$$= \frac{1}{2}m\begin{bmatrix}\dot{x}\\\dot{y}\end{bmatrix}^T \boldsymbol{M}(x,y)\begin{bmatrix}\dot{x}\\\dot{y}\end{bmatrix}.$$

The potential energy is given by

$$V(x,y) = E_{\text{potential}} = mgz = mgH(x,y)$$

$$V(x,y) = mg\left(\alpha(x^2 + y^2) - \beta\left(\sqrt{x^2 + \gamma} + \sqrt{y^2 + \gamma}\right) - \xi xy + H_0\right). \tag{6}$$

The Lagrangian is given by

$$\mathcal{L}(x,y,v_x,v_y) = T(x,y,v_x,v_y) - V(x,y)$$

$$= \frac{1}{2}\frac{7}{5}m\left(v_x^2 + v_y^2 + (H_xv_x + H_yv_y)^2\right) - mg\left(\alpha(x^2 + y^2) - \beta\left(\sqrt{x^2 + \gamma} + \sqrt{y^2 + \gamma}\right) - \xi xy + H_0\right) \tag{7}$$

---

*Corresponding author: shiba@vt.edu

where we have substituted $v_x = \dot{x}$ and $v_y = \dot{y}$. In absence of non-conservative forces such as damping or external forcing, Lagrange's equations of motion gives

$$\dot{v}_x(1 + H_x^2) + \dot{v}_y H_x H_y = - H_x \left[\frac{5}{7}g + H_{xx}v_x^2 + 2H_{xy}v_x v_y + H_{yy}v_y^2 \right] \tag{8}$$

$$\dot{v}_y(1 + H_y^2) + \dot{v}_x H_x H_y = - H_y \left[\frac{5}{7}g + H_{xx}v_x^2 + 2H_{xy}v_x v_y + H_{yy}v_y^2 \right] \tag{9}$$

where the phase space is $X = (x, y, v_x, v_y) \in \mathbb{R}^4$, $H_x = \frac{\partial H}{\partial x}$, $H_y = \frac{\partial H}{\partial y}$, etc. In the first order form, we have

$$\begin{aligned} \dot{x} &= v_x \\ \dot{y} &= v_y \\ \dot{v}_x &= - hH_x \\ \dot{v}_y &= - hH_y \end{aligned} \tag{10}$$

where

$$h \equiv h(x, y, v_x, v_y) = \frac{\frac{5}{7}g + H_{xx}v_x^2 + 2H_{xy}v_x v_y + H_{yy}v_y^2}{1 + H_x^2 + H_y^2} \tag{11}$$

Symmetries.— We note that the equations of motion (10) have the following discrete symmetry

$$s_0 : (x, y, v_x, v_y, t) \rightarrow (-x, -y, -v_x, -v_y, t) \qquad \text{that is, reflection about the origin,} \tag{12}$$

$$s_r : (x, y, v_x, v_y, t) \rightarrow (y, x, v_y, v_x, t) \qquad \text{that is, reflection about the } y = x \text{ line.} \tag{13}$$

So if $(x(t), y(t), v_x(t), v_y(t))$ is a solution to (10), then $(-x(t), -y(t), -v_x(t), -v_y(t))$ is another solution, and if $(x(t), y(t), v_x(t), v_y(t))$ is a solution to (10), then $(y(t), x(t), v_y(t), v_x(t))$ is another solution. These two symmetries, (12) and (13), can be composed to give a third symmetry, where the order of composition does not matter $(s_0 \circ s_r = s_r \circ s_0)$

$$s_0 \circ s_r : (x, y, v_x, v_y, t) \rightarrow (-y, -x, -v_y, -v_x, t) \tag{14}$$

This symmetry corresponds to reflection about the $y = -x$ line. For the conservative dynamics, the equations of motion (10) also admit a time-reversal symmetry,

$$s_t : (x, y, v_x, v_y, t) \rightarrow (x, y, v_x, v_t, -t) \tag{15}$$

Similar proposition about the solution and composition of symmetry also holds.

The corresponding Hamiltonian for the Lagrangian can be obtained via the usual Legendre transformation. Thus, the Hamiltonian is given by

$$\mathcal{H}(x, y, p_x, p_y) = T(x, y, p_x, p_y) + V(x, y) = \frac{1}{2}\mathbf{p}^T \mathbf{M}^{-1}(\mathbf{r})\mathbf{p} + V(x, y) \tag{16}$$

where the generalized momenta $\mathbf{p} = (p_x, p_y)$ are

$$\mathbf{p} = \mathbf{M}\dot{\mathbf{r}} \tag{17}$$

$$\begin{bmatrix} p_x \\ p_y \end{bmatrix} = \frac{7}{5} \begin{bmatrix} (1 + H_x^2)\dot{x} & H_x H_y \dot{y} \\ H_x H_y \dot{x} & (1 + H_y^2)\dot{y} \end{bmatrix} \tag{18}$$

where $\dot{\mathbf{r}} = (\dot{x}, \dot{y})$ and

$$\mathbf{M}^{-1}(\mathbf{r}) = \frac{5}{7} \frac{1}{1 + H_x^2 + H_y^2} \begin{bmatrix} (1 + H_y^2) & -H_x H_y \\ -H_x H_y & (1 + H_x^2) \end{bmatrix} \tag{19}$$

So, the Hamiltonian is

$$\mathcal{H}(x, y, p_x, p_y) = \frac{1}{2}\frac{5}{7} \frac{(1 + H_y^2)p_x^2 + (1 + H_x^2)p_y^2 - 2H_x H_y p_x p_y}{1 + H_x^2 + H_y^2} + V(x, y) \tag{20}$$

Energy surface.— The solutions of Eqn. (10), that is the dynamics in absence of non-conservative forces, conserve the (Jacobi constant) energy, which since the kinetic energy is quadratic in the velocities is simply the sum of kinetic energy and potential energy

$$\mathcal{E}(\mathbf{r}, \mathbf{v}) = \frac{1}{2}\mathbf{v}^T \mathbf{M}(\mathbf{r})\mathbf{v} + V(\mathbf{r}) \tag{21}$$

$$\mathcal{E}(x, y, v_x, v_y) = \frac{1}{2}\frac{7}{5} \left((1 + H_x^2)v_x^2 + (1 + H_y^2)v_y^2 + 2H_x H_y v_x v_y \right) + V(x, y) \tag{22}$$
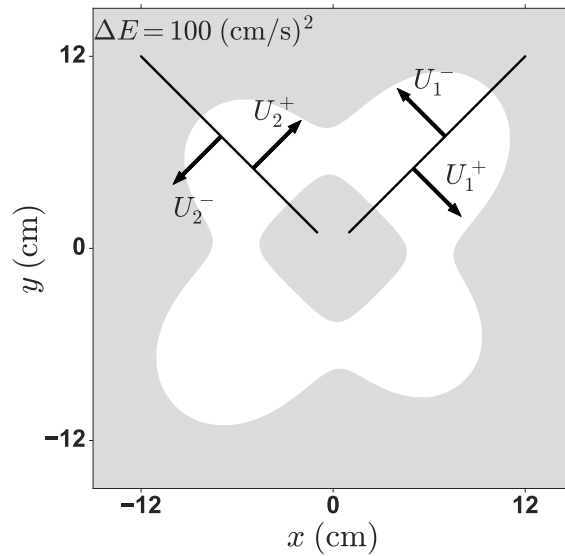
Figure S1: Hill's region for excess energy, $\Delta E = 100$ (cm/s)^2. The energetically accessible region is shown in white, and the surfaces-of-sections are marked with arrow pointing in the direction of motion that a trajectory is recorded when crossing the surface.

Let $\mathcal{M}$ be the *energy manifold* or *energy surface* given by setting the energy integral (22) equal to a constant, that is

$$\mathcal{M}(E) = \left\{ (x, y, v_x, v_y) | \mathcal{E}(x, y, v_x, v_y) = E \right\} \tag{23}$$

where E is a constant. For a fixed total energy, E, the surface $\mathcal{M}(E)$ is a three-dimensional surface embedded in the four-dimensional phase space.

Hill's Region.— The projection of the energy surface onto configuration space, the (x, y) plane, is the region of energetically possible motion for a ball of energy, E. Let $M(E)$ denote this projection, [1]

$$M(E) = \left\{ (x, y) | V(x, y) \leqslant E \right\}, \tag{24}$$

and is known historically in mechanics, as the *Hill's region*. The boundary of $M(E)$ is known as the *zero velocity curve*, and plays an important role in placing bounds on the motion of the ball. A consequence of the s_t symmetry is that any trajectory which touches the zero velocity curve (those corresponding to $V(x, y) = E$), that is the outer boundary of the energetically permissible, white region, at time t_0 must retrace its path in configuration space, $q = (x, y)$,

$$q(-t + t_0) = q(t + t_0) \tag{25}$$
$$\dot{q}(-t + t_0) = -\dot{q}(t + t_0) \tag{26}$$

Surface-of-section.— We define four topologically distinct Poincaré surfaces-of-sections as

$$U_1^\pm = \left\{ (x, v_x) \mid y - x = 0, y > 0, -\text{sign}(v_y - v_x) = \pm 1 \right\} \tag{27}$$
$$U_2^\pm = \left\{ (x, v_x) \mid y + x = 0, y > 0, \text{sign}(v_y + v_x) = \pm 1 \right\} \tag{28}$$

where U_1 and U_2 are in quadrant 1 and quadrant 2 of the (x, y) plane, while $+$ and $-$ denote motion to the right and left, respectively. A simple algebraic manipulation yields the condition that motion to the right is $v_y < v_x$ and motion to the left is $v_x < v_y$. Furthermore, we note that the function $H(x, y)$ has two discrete symmetries: it is symmetric about the origin, $H(-x, -y) = H(x, y)$, and with respect to the reflection about the $y = x$ or 45 deg line, $H(y, x) = H(x, y)$. Due to the symmetry of this rolling surface, $H(x, y)$, motion in the quadrant 1 and quadrant 2 is equivalent to the motion in the quadrant 3 and quadrant 4, respectively. We use this symmetry to increase the transition data in experiment, and to reduce the numerical computation.

---

[1] Note that our convention is to use script letters for a region in the energy surface (including the energy surface itself, $\mathcal{M}$) and italicized capital letters for that region's projection onto the configuration space (e.g., M)

2 Transition fraction

Change of Coordinates.— To simplify the expressions and analysis, we introduce polar coordinates (r, θ) via the transformation

$$x = r \cos \theta$$
$$y = r \sin \theta \tag{29}$$

and thus

$$\dot{x} = \dot{r} \cos \theta - r \dot{\theta} \sin \theta$$
$$\dot{y} = \dot{r} \sin \theta + r \dot{\theta} \cos \theta \tag{30}$$

or

$$\begin{bmatrix} v_x \\ v_y \end{bmatrix} = \begin{bmatrix} \cos \theta & -r \sin \theta \\ \sin \theta & r \cos \theta \end{bmatrix} \begin{bmatrix} \dot{r} \\ \dot{\theta} \end{bmatrix} \tag{31}$$

So the kinetic energy can be expressed as

$$T(x, y, v_x, v_y) = \frac{1}{2} \begin{bmatrix} v_x \\ v_y \end{bmatrix}^T \mathbf{M} \begin{bmatrix} v_x \\ v_y \end{bmatrix} \tag{32}$$

$$= \frac{1}{2} \begin{bmatrix} \dot{r} \\ \dot{\theta} \end{bmatrix}^T \begin{bmatrix} \cos \theta & \sin \theta \\ -r \sin \theta & r \cos \theta \end{bmatrix} \mathbf{M} \begin{bmatrix} \cos \theta & -r \sin \theta \\ \sin \theta & r \cos \theta \end{bmatrix} \begin{bmatrix} \dot{r} \\ \dot{\theta} \end{bmatrix} \tag{33}$$

$$= \frac{1}{2} \begin{bmatrix} \dot{r} \\ \dot{\theta} \end{bmatrix}^T \tilde{\mathbf{M}} \begin{bmatrix} \dot{r} \\ \dot{\theta} \end{bmatrix} \tag{34}$$

So, the conjugate momenta $\tilde{\mathbf{p}} = (p_r, p_\theta)$ is given by

$$\begin{bmatrix} p_r \\ p_\theta \end{bmatrix} = \frac{7}{5} \begin{bmatrix} \cos \theta & \sin \theta \\ -r \sin \theta & r \cos \theta \end{bmatrix} \begin{bmatrix} (1 + H_x^2) & H_x H_y \\ H_x H_y & (1 + H_y^2) \end{bmatrix} \begin{bmatrix} \cos \theta & -r \sin \theta \\ \sin \theta & r \cos \theta \end{bmatrix} \begin{bmatrix} \dot{r} \\ \dot{\theta} \end{bmatrix} \tag{35}$$

$$= \frac{7}{5} \begin{bmatrix} \cos \theta & \sin \theta \\ -r \sin \theta & r \cos \theta \end{bmatrix} \begin{bmatrix} (1 + H_x^2) & H_x H_y \\ H_x H_y & (1 + H_y^2) \end{bmatrix} \begin{bmatrix} v_x \\ v_y \end{bmatrix} \tag{36}$$

On the Poincaré surface-of-section, U_1, $\theta = \pi/4$, so $\cos \theta = 1/\sqrt{2}$ and $\sin \theta = 1/\sqrt{2}$. Thus, on this section, we have

$$\begin{bmatrix} p_r \\ p_\theta \end{bmatrix} = \frac{7}{5} \frac{1}{\sqrt{2}} \begin{bmatrix} 1 & 1 \\ -r & r \end{bmatrix} \begin{bmatrix} (1 + H_x^2) & H_x H_y \\ H_x H_y & (1 + H_y^2) \end{bmatrix} \begin{bmatrix} v_x \\ v_y \end{bmatrix} \tag{37}$$

$$= \frac{7}{5} \frac{1}{\sqrt{2}} \begin{bmatrix} 1 & 1 \\ -r & r \end{bmatrix} \begin{bmatrix} v_x(1 + H_x^2) + v_y H_x H_y \\ v_x H_x H_y + v_y(1 + H_y^2) \end{bmatrix} \tag{38}$$

$$= \frac{7}{5} \frac{1}{\sqrt{2}} \begin{bmatrix} v_x(1 + H_x^2) + v_y H_x H_y + v_x H_x H_y + v_y(1 + H_y^2) \\ -r \left\{ v_x(1 + H_x^2) + v_y H_x H_y - v_x H_x H_y - v_y(1 + H_y^2) \right\} \end{bmatrix} \tag{39}$$

Now, on the Poincaré surface-of-section, U_1, $y = x$, $y > 0$, and $r = \sqrt{2}y$, and thus

$$H(x, y)|_{U_1} = H(y, y) = 2\alpha y^2 - 2\beta \sqrt{y^2 + \gamma} - \xi y^2 + H_0 \tag{40}$$

$$H_x(x, y)|_{U_1} = H_y(x, y)|_{U_1} = H_y(y, y) = 4\alpha y - 2\beta \frac{y}{\sqrt{y^2 + \gamma}} - 2\xi y \tag{41}$$

$$H_r(r) = 2\alpha r - \beta \frac{r}{\sqrt{\frac{r^2}{2} + \gamma}} - \xi r = 2\sqrt{2}\alpha y - \beta \frac{\sqrt{2}y}{\sqrt{y^2 + \gamma}} - \sqrt{2}\xi y \tag{42}$$

$$H_r(r) = \frac{H_y}{\sqrt{2}} = \frac{H_x}{\sqrt{2}} \tag{43}$$

On the Poincaré surface-of-section, U_1, the conjugate momenta is given by

$$\begin{bmatrix} p_r \\ p_\theta \end{bmatrix} = \frac{7}{5} \frac{1}{\sqrt{2}} \begin{bmatrix} v_x(1 + H_x^2) + v_y H_x H_y + v_x H_x H_y + v_y(1 + H_y^2) \\ -r \left\{ v_x(1 + H_x^2) + v_y H_x H_y - v_x H_x H_y - v_y(1 + H_y^2) \right\} \end{bmatrix} \tag{44}$$

$$= \frac{7}{5} \frac{1}{\sqrt{2}} \begin{bmatrix} (v_x + v_y)(1 + 4H_r^2) \\ -r(v_x - v_y) \end{bmatrix} \tag{45}$$

This can be solved to express v_x, v_y as

$$v_x = \frac{5}{7}\frac{1}{\sqrt{2}}\left(\frac{p_r}{(1+4H_r^2)} - \frac{p_\theta}{r}\right) \tag{46}$$

$$v_y = \frac{5}{7}\frac{1}{\sqrt{2}}\left(\frac{p_r}{(1+4H_r^2)} + \frac{p_\theta}{r}\right) \tag{47}$$

In polar coordinates, the condition

$$-\text{sign}(v_y - v_x) = \pm 1 \tag{48}$$

gives, using Eqns. 46 and 47,

$$-\text{sign}\left[\frac{5}{7}\frac{1}{\sqrt{2}}\left(\frac{p_r}{(1+4H_r^2)} + \frac{p_\theta}{r}\right) - \frac{5}{7}\frac{1}{\sqrt{2}}\left(\frac{p_r}{(1+4H_r^2)} - \frac{p_\theta}{r}\right)\right] = \pm 1 \tag{49}$$

which simplifies to

$$-\text{sign}\left(p_\theta\right) = \pm 1 \tag{50}$$

Similarly, we can obtain the condition for the surface-of-section, U_2. Thus, in polar coordinates, we have Poincaré surface-of-sections

$$U_1^\pm = \{(r, p_r) \mid \theta = \pi/4, \ -\text{sign}(p_\theta) = \pm 1\} \tag{51}$$
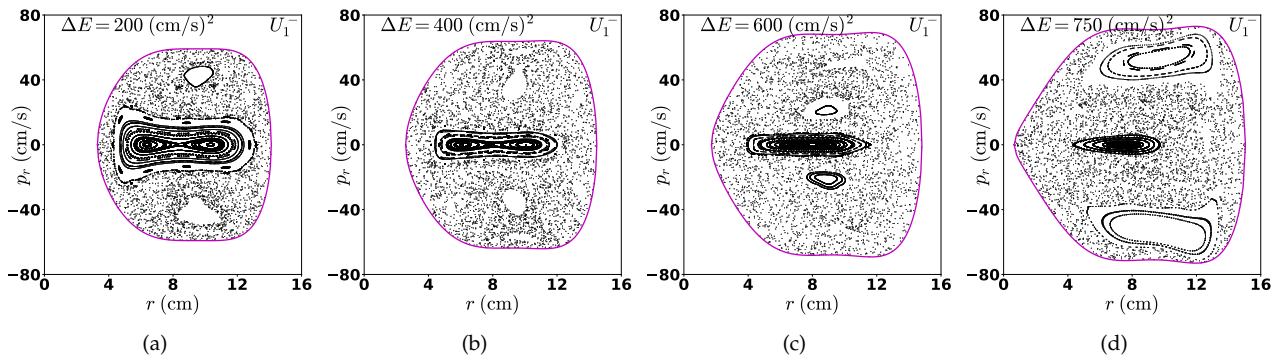

Figure S2: Poincaré surface-of-section of trajectories at energy above the critical value of $E_e = 3304.24$ (cm/s)^2. The global dynamics has characteristics of chaos while trajectories transition between wells and cross the surface-of-section, U_1^-. A movie (same as Fig. 3 in the primary manuscript) showing the Poincaré section for a range of excess energy can be found here.

Using the above transformations, we obtain the solutions of Eqn. 10 in cartesian coordinates and transform it to polar coordinate for further analysis. These closed curves on the Poincaré section has been called *reactive islands* in the context of chemical reactions since trajectories that enter these islands evolve from the "reactant" to "product" side on the energy surface [2, 3, 4, 5, 16]. We also note that the total energy, on the Poincaré SOS U_1, is given by

$$\mathcal{E}(x, y, v_x, v_y) = \frac{1}{2}\frac{7}{5}\left[\left(1 + H_x^2\right)\left(v_x^2 + v_y^2\right) + 2H_x^2 v_x v_y\right] + gH(x, y) \tag{52}$$

$$\mathcal{E}(r, p_r, p_\theta) = \frac{1}{2}\frac{5}{7}\left[\frac{p_r^2}{(1+4H_r^2)} + \frac{p_\theta^2}{r^2}\right] + gH(r) \tag{53}$$

and the boundary of the energy surface $\mathcal{E} = E$ on U_1 is given by $p_\theta = 0$, so

$$p_r = \pm\sqrt{\frac{14}{5}(E - gH(r))(1 + 4H_r^2)} \tag{54}$$

so the symplectic area of the energy surface on the SOS U_1 is

$$A_E = 2\int_{r_{\min}}^{r_{\max}}\sqrt{\frac{14}{5}(E - gH(r))(1 + 4H_r^2)}\ dr = 2\int_{r_{\min}}^{r_{\max}} f(r; E)\ dr \tag{55}$$

where $r_{\min}$ and $r_{\max}$ are the two positive roots of $E - gH(r) = 0$ for the energy value E. According to [10], the area of the transitioning region, for small excess energy ΔE is

$$A_{\text{trans}} = T_{\text{po}}\Delta E \tag{56}$$

where $T_{\text{po}} = 2\pi/\omega$ is the period of the unstable periodic orbit within the bottleneck, whose stable and unstable manifolds act as the pathways for the ball to transition between the quadrants. We note that the ω can be obtained analytically, as the saddle point has eigenvalues $\pm\lambda$ and $\pm i\omega$, thus ω can be written in terms of the parameters which define the surface.

The symplectic area of the transitioning trajectories grows linearly in ΔE. If we write $E = \Delta E + E_e$, and perform Taylor expansion of $f(r; E)$ about E_e

$$f(r; E) = f(r; E_e) + \left.\frac{\partial f}{\partial E}\right|_{E_e} \Delta E + \mathcal{O}(\Delta E^2) \tag{57}$$

$$A_E = 2 \int_{r_{\min}}^{r_{\max}} f(r; E_e)\, dr + \left(2 \int_{r_{\min}}^{r_{\max}} \left.\frac{\partial f}{\partial E}\right|_{E_e} dr \right) \Delta E + \mathcal{O}(\Delta E^2) \tag{58}$$

$$A_E = A_0 + \tau \Delta E \tag{59}$$

where

$$A_0 = 2 \int_{r_{\min}}^{r_{\max}} f(r; E_e)\, dr = 2 \int_{r_{\min}}^{r_{\max}} \sqrt{\frac{14}{5}(E_e - gH(r))(1 + 4H_r^2)}\, dr \tag{60}$$

$$\tau = 2 \int_{r_{\min}}^{r_{\max}} \left.\frac{\partial f}{\partial E}\right|_{E_e} dr = 2 \int_{r_{\min}}^{r_{\max}} \frac{1}{2} \sqrt{\frac{14}{5}\frac{(1 + 4H_r^2)}{(E_e - gH(r))}}\, dr = \int_{r_{\min}}^{r_{\max}} \sqrt{\frac{14}{5}\frac{(1 + 4H_r^2)}{(E_e - gH(r))}}\, dr \tag{61}$$

So,

$$A_E = A_0 \left(1 + \frac{\tau}{A_0}\Delta E \right) \tag{62}$$

Thus, the transition fraction is

$$p_{\text{trans}} = \frac{A_{\text{trans}}}{A_E} = \frac{T_{\text{po}}\Delta E}{A_0 \left(1 + \frac{\tau}{A_0}\Delta E \right)} \tag{63}$$

$$\approx \frac{T_{\text{po}}}{A_0}\Delta E \left(1 - \frac{\tau}{A_0}\Delta E + \mathcal{O}(\Delta E^2) \right) \tag{64}$$

So for small excess energy ΔE, the growth in p_{trans} with ΔE is linear, with slope T_{po}/A_0.

3 Phase space conduits leading to transition

We consider the dynamics of conservative system by determining the phase space skeleton that governs transition between potential well (or, equivalently escape from a well). In the simplest case of only two degrees of freedom, the phase space is of 4 dimensional and the boundary between potential wells is defined using unstable periodic orbit that lie in the bottleneck connecting the wells. This has also been called a transition state in chemical reaction dynamics and form the boundary of a dividing surface used in calculation of reaction rates [4, 6, 7, 8, 12, 16]. The set of all states leading to escape from a potential well can be understood as residing within an invariant manifold of geometry $\mathbb{R}^1 \times \mathbb{S}^1$, that is a cylinder or tube. The interior of this tube defines the set of all states which will transition to the adjacent well.

3.1 Linearization near the rank one saddle

It is to be noted that the linearization of the behavior of trajectories near the saddle-center equilibrium points appears in the leading order expression of the transition fraction (64). We are interested in trajectories which have an energy just above that of the critical value. As shown in Fig. 1, the region of possible motion for $E > E_e$ contains a neck around each saddle equilibrium point. The geometry of trajectories close to the neck region is studied by considering the linearized equations of motion near the equilibrium point.

In this section, let $\mathbf{x}_{e,1-2}$ denote the saddle equilibrium point between quadrant 1 and 2. Furthermore, for a fixed energy E, we consider a neighborhood of $\mathbf{x}_{e,1-2}$ on the energy surface, whose configuration space projections are the neck regions described previously. We refer to this neighborhood as the *equilibrium region* and

denote it by $\mathcal{R}$ on the energy surface. We perform a coordinate transformation with $\mathbf{x}_{e,1-2} = (x_{e,1-2}, y_{e,1-2}, 0, 0)$ as the new origin, and keeping only the linear terms, we obtain

$$\dot{\mathbf{x}} = D\mathbf{f}\big|_{(x_{e,1-2}, y_{e,1-2}, 0, 0)} \mathbf{x} \qquad \text{where,} \qquad \mathbf{x} = [x, y, v_x, v_y]^T \tag{65}$$

The Jacobian involves derivatives of Eqns. (1) and (11), and can be written compactly as

$$D\mathbf{f}(x, y, v_x, v_y) = \begin{pmatrix} 0 & 0 & 1 & 0 \\ 0 & 0 & 0 & 1 \\ -h_x H_x - h H_{xx} & -h_y H_x - h H_{xy} & -h_{v_x} H_x & -h_{v_y} H_x \\ -h_x H_y - h H_{xy} & -h_y H_y - h H_{yy} & -h_{v_x} H_y & -h_{v_y} H_y \end{pmatrix} \tag{66}$$

The eigenvalues of the linearized equations are of the form $\pm\lambda$ and $\pm i\omega$ with corresponding eigenvectors u_1, u_2, w_1, w_2, where $\lambda > 0$, $\omega > 0$. Thus, the general (real) solution of (65) has the form

$$\mathbf{x}(t) = (x(t), y(t), v_x(t), v_y(t)) = \alpha_1 e^{\lambda t} u_1 + \alpha_2 e^{\lambda t} u_2 + 2Re(\beta e^{i\omega t} w_1) \tag{67}$$

where, α_1, α_2 are real and $\beta = \beta_1 + i\beta_2$ is complex. It is to be noted that the time period of small oscillation near the saddle equilibrium point is given by $T_{\text{po}} = 2\pi/\omega$ which appears in the leading order expression of the transition fraction in Eqn. (64) and phase space flux in [10]. This general solution classifies solutions on the energy surface into different classes upon the limiting behavior of position coordinates as $t \to \pm\infty$ in the linearized system, as discussed in [1, 9]. By virtue of Moser's generalization of a theorem of Lyapunov on Hamiltonian system with only a pair of real eigenvalues and other complex eigenvalues, we can extend all the qualitative results of the linearized solution near the equilibrium points to the full nonlinear equations [14, 15, 18].

Boundary between transition and non-transition trajectories.— The key observation from the analysis above is that the asymptotic orbits are pieces of the stable and unstable cylindrical manifolds of the periodic orbit and they separate two distinct types of motion: transit and non-transit. The transitition trajectories, passing from one potential well to another, are those inside the cylindrical manifolds, or tube. The non-transit orbits, which bounce back to their realm of origin, are those outside the tube.

This observation will be important for the numerical construction of sets of trajectories which transition from a potential well. Emanating from the unstable periodic orbits in these neck regions are their stable and unstable manifolds with a $\mathbb{R}^1 \times S^1$ geometry. The cylinders, or tubes, have the physical property that all motion through the bottleneck in which the periodic orbit resides must occur through the interior of these surfaces. The tubes thus act as phase space conduits for the trajectories to travel between large zones of the energy surface, that is realms, which are separated by the bottlenecks.

3.2 Computational approach for finding regions of imminent transition

Step 1: Select appropriate energy above the critical value. For computation of manifolds that act as *boundary* between the transition and non-transition trajectories, we select the total energy, E, above the critical value and so the excess energy $\Delta E > 0$. This excess energy can be arbitrarily large as long as the energy manifold corresponding to the energy stays within the dynamical system's phase space bounds.

Step 2: Compute the unstable periodic orbit associated with the rank one saddle. We consider a procedure which computes periodic orbits around in a relatively straightforward fashion. This procedure begins with small "seed" initial conditions obtained from the linearized equations of motion near $\mathbf{x}_{e,1-2}$, and uses differential correction and numerical continuation to generate the desired periodic orbit corresponding to the chosen energy E [9]. The result is a periodic orbit of the desired energy E of some period T, which will be close to $2\pi/\omega$ where $\pm\omega$ is the imaginary pair of eigenvalues of the linearization around the saddle point.

Initial guess for periodic orbit. — The linearized equations of motion near an equilibrium point can be used to initialize a guess for the differential correction method. Let us select the equilibrium point, $\mathbf{x}_{eq,1-2}$, for the purpose of illustration and the transition fraction results presented in the main article. The linearization yields an eigenvalue problem $Av = \gamma v$, where A is the Jacobian matrix evaluated at the equilibrium point, γ is the eigenvalue, and $v = [k_1, k_2, k_3, k_4]^T$ is the corresponding eigenvector. Thus, using the structure of A from Eqn. (66) we can write

$$\begin{aligned} k_3 &= \gamma k_1 \\ k_4 &= \gamma k_2 \\ ak_1 + bk_2 &= \gamma k_3 \\ ck_1 + dk_2 &= \gamma k_4 \end{aligned} \tag{68}$$

So when $\gamma = \pm\lambda$, which correspond to the hyperbolic directions of the rank-1 saddle, the corresponding eigenvectors are given by

$$u_1 = [1, k_2, \lambda, \lambda k_2]$$
$$u_2 = [1, k_2, -\lambda, -\lambda k_2]$$

(69)

and when $\gamma = \pm i\omega$, which correspond to the center directions, the corresponding eigenvectors are given by

$$w_1 = [1, k_2, i\omega, i\omega k_2]$$
$$w_2 = [1, k_2, -i\omega, -i\omega k_2]$$

(70)

where, $k_2 = (\gamma^2 - a)/b$ is the constant depending on the eigenvalue, γ, and the entries of Jacobian, $a = -h_x H_x - h H_{xx}$ and $b = -h_y H_x - h H_{xy}$, are evaluated at the equilibrium point $(x_{e,1-2}, y_{e,1-2}, 0, 0)$. Thus, the general solution of linearized equation of motion in Eqn. (67) can be used to initialize a guess for the periodic orbit for a small amplitude, $A_x << 1$. Let $\beta = -A_x/2$ and using the eigenvector along the center direction we can guess the initial condition to be

$$\bar{\mathbf{x}}_{0,g} = (x_{e,1-2}, y_{e,1-2}, 0, 0)^T + 2Re(\beta w_1) = (x_{e,1-2} - A_x, y_{e,1-2} - A_x k_2, 0, 0)^T$$

(71)

Differential correction of the initial condition.— In this procedure, we attempt to introduce small change in the initial guess such that the periodic orbit $\bar{\mathbf{x}}_{po}$

$$\left\| \bar{\mathbf{x}}_{po}(T) - \bar{\mathbf{x}}_{po}(0) \right\| < \epsilon$$

(72)

for some tolerance $\epsilon << 1$. In this approach, we hold $x-$coordinate constant, while applying correction to the initial guess of the $y-$coordinate, use v_y-coordinate for terminating event-based integration, and v_x-coordinate to test convergence of the periodic orbit. It is to be noted that this combination of coordinates is suitable for the structure of initial guess at hand, and in general will require some permutation of the phase space coordinates to achieve a stable algorithm.

Let us denote the flow map of a differential equation $\dot{\mathbf{x}} = \mathbf{f}(\mathbf{x})$ with initial condition $\mathbf{x}(t_0) = \mathbf{x}_0$ by $\phi(t; \mathbf{x}_0)$. Thus, the displacement of the final state under a perturbation δt becomes

$$\delta\bar{\mathbf{x}}(t + \delta t) = \phi(t + \delta t; \bar{\mathbf{x}}_0 + \delta\bar{\mathbf{x}}_0) - \phi(t; \bar{\mathbf{x}}_0)$$

(73)

with respect to the reference orbit $\bar{\mathbf{x}}(t)$. Thus, measuring the displacement at $t_1 + \delta t_1$ and expanding into Taylor series gives

$$\delta\bar{\mathbf{x}}(t_1 + \delta t_1) = \frac{\partial\phi(t_1; \bar{\mathbf{x}}_0)}{\partial\mathbf{x}_0}\delta\bar{\mathbf{x}}_0 + \frac{\partial\phi(t_1; \bar{\mathbf{x}}_0)}{\partial t_1}\delta t_1 + h.o.t$$

(74)

where the first term on the right hand side is the state transition matrix, $\mathbf{\Phi}(t_1, t_0)$, when $\delta t_1 = 0$. Thus, it can be obtained as numerical solution to the variational equations as discussed in [17]. Let us suppose we want to reach the desired point $\mathbf{x}_d$, we have

$$\bar{\mathbf{x}}(t_1) = \phi(t_1; \bar{\mathbf{x}}_0) = \bar{\mathbf{x}}_1 = \mathbf{x}_d - \delta\bar{\mathbf{x}}_1$$

(75)

which has an error $\delta\bar{\mathbf{x}}_1$ and needs correction. This correction to the first order can be obtained from the state transition matrix at t_1 and an iterative procedure of this small correction based on first order yields convergence in few steps. For the equilibrium point under consideration, we initialize the guess as

$$\bar{\mathbf{x}}(0) = (x_{0,g}, y_{0,g}, 0, 0)^T$$

(76)

and using numerical integrator we continue until next $v_x = 0$ event crossing with a high pecified tolerance (typically 10^{-14}). So, we obtain $\bar{\mathbf{x}}(t_1)$ which for the guess periodic orbit denotes the half-period point, $t_1 = T_{0,g}/2$ and compute the state transition matrix $\mathbf{\Phi}(t_1, 0)$. This can be used to correct the initial value of $y_{0,g}$ to approximate the periodic orbit while keeping $x_{0,g}$ constant. Thus, correction to the first order is given by

$$\delta v_{x_1} = \Phi_{32}\delta y_0 + \dot{v}_{x_1}\delta t_1 + h.o.t$$

(77)

$$\delta v_{y_1} = \Phi_{42}\delta y_0 + \dot{v}_{y_1}\delta t_1 + h.o.t$$

(78)

where Φ_{ij} is the $(i,j)^{th}$ entry of $\mathbf{\Phi}(t_1, 0)$ and the acceleration terms come from the equations of motion evaluated at the crossing $t = t_1$ when $v_{x_1} = \delta v_{x_1} = 0$. Thus, we obtain the first order correction δy_0 as

$$\delta y_0 \approx \left(\Phi_{42} - \Phi_{32}\frac{\dot{v}_{y_1}}{\dot{v}_{x_1}} \right)^{-1} \delta v_{y_1}$$

(79)

$$y_0 \rightarrow y_0 - \delta y_0$$

(80)

which is iterated until $|v_{y_1}| = |\delta v_{y_1}| < \epsilon$ for some tolerance ϵ, since we want the final periodic orbit to be of the form

$$\bar{\mathbf{x}}_{t_1} = (x_1, y_1, 0, 0)^T \tag{81}$$

This procedure yields an accurate initial condition for a periodic orbit of small amplitude $A_x << 1$, since our initial guess is based on the linear approximation near the equilibrium point. It is also to be noted that differential correction assumes the guess periodic orbit has a small error (for example in this system, of the order of 10^{-2}) and can be corrected using first order form of the correction terms. If, however, larger steps in correction are applied this can lead to unstable convergence as the half-orbit overshoots between successive steps. Even though there are other algorithms for detecting unstable periodic orbits, differential correction is easy to implement and shows reliable convergence for generating a dense family of periodic orbits at arbitrary high excess energy near the rank-1 saddle.

Numerical continuation to periodic orbit at arbitrary energy.— The above procedure yields an accurate initial condition for a periodic orbit from a single initial guess. If our initial guess came from the linear approximation near the equilibrium point, from Eqn. (67), it has been observed numerically that we can only use this procedure for small amplitude, of order 10^{-4}, for the chosen parameters in (1), periodic orbits around $\mathbf{x}_{e,1-2}$. This small amplitudes correspond to small excess energy, typically of the order 10^{-2} (cm/s)^2, and if we want a periodic orbit of arbitrarily large amplitude, we need to use numerical continuation to generate a family which reaches the appropriate energy E. This is performed using two nearby periodic orbits of small amplitude. To this end, we proceed as follows. Suppose we find two small nearby periodic orbit initial conditions, $\bar{\mathbf{x}}_0^{(1)}$ and $\bar{\mathbf{x}}_0^{(2)}$, correct to within the tolerance d, using the differential correction procedure described above. We can generate a family of periodic orbits with successively increasing amplitudes around $\bar{\mathbf{x}}_{e,1-2}$ in the following way. Let

$$\Delta = \bar{\mathbf{x}}_0^{(2)} - \bar{\mathbf{x}}_0^{(1)} = [\Delta x_0, \Delta y_0, 0, 0]^T \tag{82}$$

A linear extrapolation to an initial guess of slightly larger amplitude, $\bar{\mathbf{x}}_0^{(3)}$ is given by

$$\bar{\mathbf{x}}_{0,g}^{(3)} = \bar{\mathbf{x}}_0^{(2)} + \Delta \tag{83}$$

$$= \left[(\mathbf{x}_0^{(2)} + \Delta x_0), (y_0^{(2)} + \Delta y_0), 0, 0 \right]^T \tag{84}$$

$$= \left[x_0^{(3)}, y_0^{(3)}, 0, 0 \right]^T \tag{85}$$

Thus, keeping $x_0^{(3)}$ fixed, we can use differential correction on this initial condition to compute an accurate solution $\bar{\mathbf{x}}_0^{(3)}$ from the initial guess $\bar{\mathbf{x}}_{0,g}^{(3)}$ and repeat the process until we have a family of solutions. We can keep track of the energy of each periodic orbit and when we have two solutions, $\bar{\mathbf{x}}_0^{(k)}$ and $\bar{\mathbf{x}}_0^{(k+1)}$, whose energy brackets the appropriate energy, E, we can resort to combining bisection and differential correction to these two periodic orbits until we converge to the desired periodic orbit to within a specified tolerance. Thus, the result is a periodic orbit at desired energy E and of some period T with an initial condition X_0.

Step 3: Computation of invariant manifolds. First, we find the local approximation to the unstable and stable manifolds of the periodic orbit from the eigenvectors of the monodromy matrix. Next, the local linear approximation of the unstable (or stable) manifold in the form of a state vector is integrated in the nonlinear equations of motion to produce the approximation of the unstable (or stable) manifolds. This procedure is known as *globalization of the manifolds* and we proceed as follows:

First, the state transition matrix $\Phi(t)$ along the periodic orbit with initial condition X_0 can be obtained numerically by integrating the variational equations along with the equations of motion from $t = 0$ to $t = T$. This is known as the monodromy matrix $M = \Phi(T)$ and the eigenvalues can be computed numerically. For Hamiltonian systems (see [13] for details), tells us that the four eigenvalues of M are of the form

$$\lambda_1 > 1, \qquad \lambda_2 = \frac{1}{\lambda_1}, \qquad \lambda_3 = \lambda_4 = 1 \tag{86}$$

The eigenvector associated with eigenvalue λ_1 is in the unstable direction, the eigenvector associated with eigenvalue λ_2 is in the stable direction. Let $e^s(X_0)$ denote the normalized (to 1) stable eigenvector, and $e^u(X_0)$ denote the normalized unstable eigenvector. We can compute the manifold by initializing along these eigenvectors as:

$$X^s(X_0) = X_0 + \epsilon e^s(X_0) \tag{87}$$

for the stable manifold at X_0 along the periodic orbit as

$$X^u(X_0) = X_0 + \epsilon e^u(X_0) \tag{88}$$

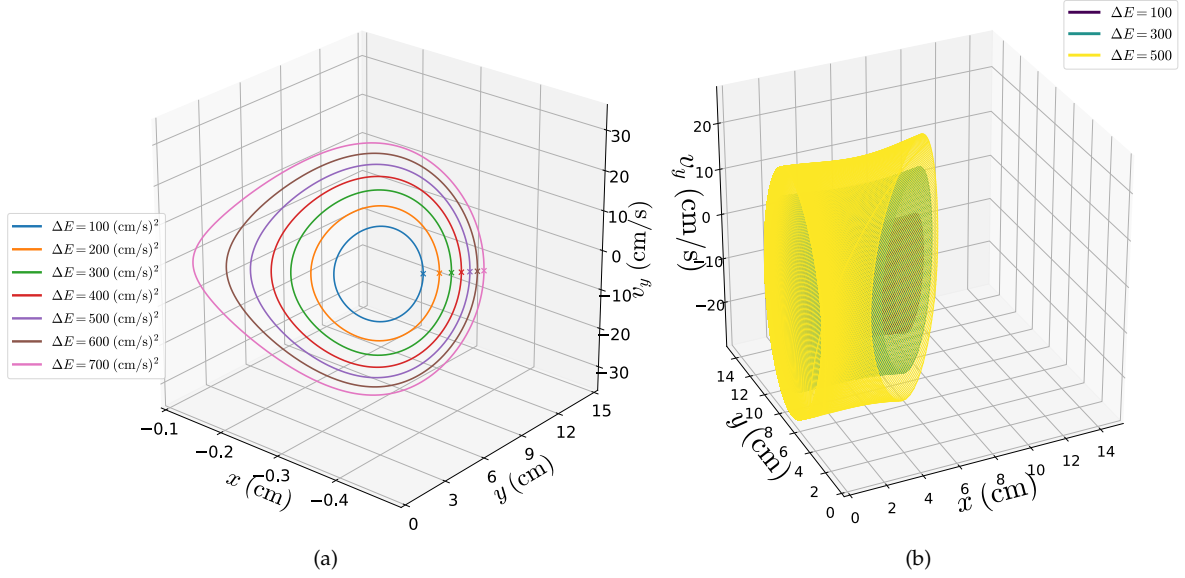Figure S3: (a) Unstable periodic orbits for excess energy, $\Delta E = 100, 200, 300, 400, 500, 600, 700$ (cm/s)^2, around the equilibrium point, $\mathbf{x}_{e,1-2}$ connecting the quadrant 1 and 2. The cross marks indicate the initial conditions obtained using differential correction, while the initial condition for high excess energy required numerical continuation. (b) Invariant manifolds for excess energy, $\Delta E = 100, 300, 500$ (cm/s)^2 that act as phase space conduits for transition trajectories to travel between potential wells. The manifolds shown here are connecting the periodic orbit around the saddle between quadrant 1 and 2 and the Poincaré section, U_1^- in the quadrant 1. For monotonically increasing values of energy, these manifolds are nested such that trajectory at a specific value of energy has to pass through the manifold at the same energy. A movie (same as Fig. 2 in the primary manuscript) showing the geometrical structure of these manifolds in the (x, y, v_y) space can be found here.

for the unstable manifold at X_0. Here the small displacement from X_0 is denoted by ϵ and its magnitude should be small enough to be within the validity of the linear estimate, yet not so small that the time of flight becomes too large due to asymptotic nature of the stable and unstable manifolds. Ref. [9] suggests typical values of $\epsilon > 0$ corresponding to nondimensional position displacements of magnitude around 10^{-6}. By numerically integrating the unstable vector forwards in time, using both ϵ and $-\epsilon$, for the forward and backward branches respectively, we generate trajectories shadowing the two branches, W_+^u and W_-^u, of the unstable manifold of the periodic orbit. Similarly, by integrating the stable vector backwards in time, using both ϵ and $-\epsilon$, for forward and backward branch respectively, we generate trajectories shadowing the stable manifold, $W_{+,-}^s$. For the manifold at $X(t)$, one can simply use the state transition matrix to transport the eigenvectors from X_0 to $X(t)$:

$$X^s(X(t)) = \Phi(t, 0) X^s(X_0) \tag{89}$$

It is to be noted that since the state transition matrix does not preserve the norm, the resulting vector must be normalized. The globalized invariant manifolds associated with rank-1 saddles are known as Conley-McGehee tubes [11]. These tubes form the skeleton of transition dynamics by acting as conduits for the states inside them to travel between potential wells.

Step 4: Compute intersection of tubes with the Poincaré surface-of-section Now an event crossing function can be used along with the numerical integration to compute intersection of the tube manifolds with the Poincaré surface-of-section, U_1^- as defined in Eqn. (27), and then transformed to polar coordinates using the transformation derived in §2. This is shown for few excess energy in Fig. S4.
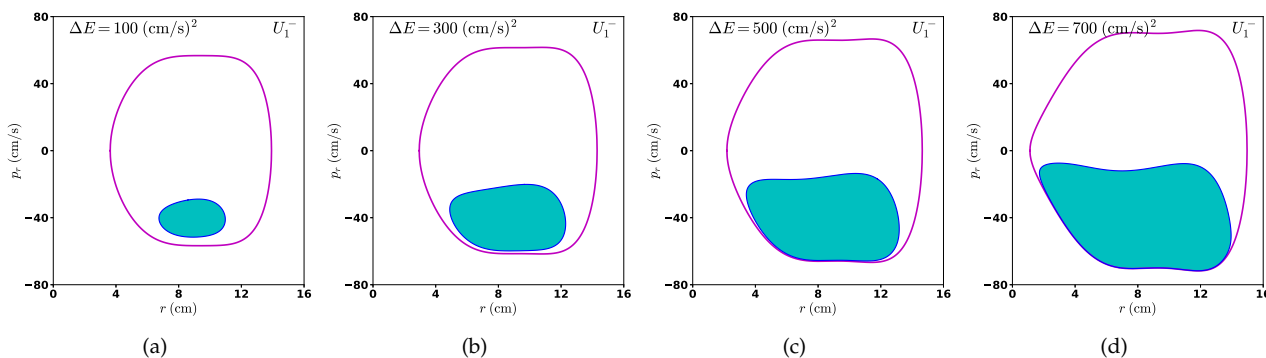
Figure S4: Shows the intersection of tube (stable) manifold and energy surface with the Poincaré SOS, U_1^-, in black and magenta, respectively, for $\Delta E = 100, 300, 500, 700$ $(\text{cm/s})^2$. The trajectories that are in the cyan region for the given energy ΔE lead to imminent transition from the quadrant 1 to 2. A movie (same as Fig. 4 in the primary manuscript) of increasing transition area on the Poincaré section, U_1^-, can be found here.

[1] C. C. Conley. Low energy transit orbits in the restricted three-body problem. *SIAM J. Appl. Math.*, 16: 732–746, 1968.

[2] N. De Leon. Cylindrical manifolds and reactive island kinetic theory in the time domain. *J. Chem. Phys.*, 96:285–297, 1992.

[3] N. De Leon and S. Ling. Simplification of the transition state concept in reactive island theory: Application to the HCN=CNH isomerization. *J. Chem. Phys.*, 101:4790–4802, 1994.

[4] N. De Leon, M. A. Mehta, and R. Q. Topper. Cylindrical manifolds in phase space as mediators of chemical reaction dynamics and kinetics. I. Theory. *J. Chem. Phys.*, 94:8310–8328, 1991.

[5] N. De Leon, M. A. Mehta, and R. Q. Topper. Cylindrical manifolds in phase space as mediators of chemical reaction dynamics and kinetics. II. Numerical considerations and applications to models with two degrees of freedom. *J. Chem. Phys.*, 94:8329–8341, 1991.

[6] F. Gabern, W. S. Koon, J. E. Marsden, and S. D. Ross. Theory and computation of non-RRKM lifetime distributions and rates in chemical systems with three or more degrees of freedom. *Physica D*, 211:391–406, 2005.

[7] C. Jaffé, D. Farrelly, and T. Uzer. Transition state in atomic physics. *Phys. Rev. A*, 60:3833–3850, 1999.

[8] C. Jaffé, D. Farrelly, and T. Uzer. Transition state theory without time-reversal symmetry: chaotic ionization of the hydrogen atom. *Phys. Rev. Lett.*, 84:610–613, 2000.

[9] W. S. Koon, M. W. Lo, J. E. Marsden, and S. D. Ross. *Dynamical systems, the three-body problem and space mission design*. Marsden books, 2011. ISBN 978-0-615-24095-4.

[10] R. S. MacKay. Flux over a saddle. *Physics Letters A*, 145:425–427, 1990.

[11] J. E. Marsden and S. D. Ross. New methods in celestial mechanics and mission design. *Bulletin of the American Mathematical Society*, 43(1):43–73, 2006.

[12] C. Clay Marston and N. De Leon. Reactive islands as essential mediators of unimolecular conformational isomerization: A dynamical study of 3-phospholene. *J. Chem. Phys.*, 91:3392–3404, 1989.

[13] K. R. Meyer, G. R. Hall, and D. Offin. *Introduction to Hamiltonian Dynamical Systems and the N-Body Problem*. Springer, 2009.

[14] J. Moser. On the generalization of a theorem of Liapunov. *Comm. Pure Appl. Math.*, 11:257–271, 1958.

[15] J. Moser. New aspects in the theory of stability of Hamiltonian systems. *Comm. Pure Appl. Math.*, 11: 81–114, 1958.

[16] A. M. Ozorio de Almeida, N. De Leon, Manish A. Mehta, and C. Clay Marston. Geometry and dynamics of stable and unstable cylinders in hamiltonian systems. *Physica D: Nonlinear Phenomena*, 46(2):265 – 285, 1990.

[17] T. S. Parker and L. O. Chua. *Practical Numerical Algorithms for Chaotic Systems*. Springer-Verlag New York, Inc., New York, NY, USA, 1989. ISBN 0-387-96689-7.

[18] S. Wiggins. *Introduction to applied nonlinear dynamical systems and chaos*. Springer, New York, 2nd ed edition, 2003. ISBN 978-0-387-00177-7.